

# Combination of Genetic Screening and Molecular Dynamics as a Useful Tool for Identification of Disease-Related Mutations: ZASP PDZ Domain G54S Mutation Case

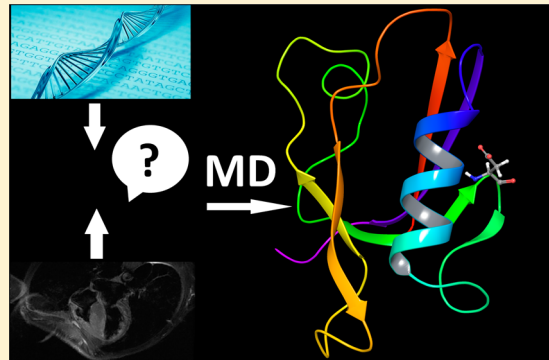
Filip Fratev,<sup>\*†‡</sup> Elina Mihaylova,<sup>‡</sup> and Ilza Pajeva<sup>†</sup>

<sup>†</sup>Institute of Biophysics and Biomedical Engineering, Bulgarian Academy of Sciences, Acad. G. Bonchev Str. Block 105, 1113 Sofia, Bulgaria

<sup>‡</sup>Micar21 Ltd., Persenk Str. 34B, 1407 Sofia, Bulgaria

Supporting Information

**ABSTRACT:** Cypher/ZASP (*LDB3* gene) is known to interact with a network of proteins. It binds to  $\alpha$ -actinin and the calcium voltage channels (LTCC) via its PDZ domain. Here we report the identification of a highly conserved ZASP G54S mutation classified as a variant of unknown significance in a sample of an adult with hypertrophic cardiomyopathy (HCM). The initial bioinformatics calculations strongly evaluated G54S as damaging. Furthermore, we employed accelerated and classical molecular dynamics and free energy calculations to study the structural impact of this mutation on the ZASP apo form and to address the question of whether it can be linked to HCM. Seventeen independent MD runs and simulations of  $2.5 \mu\text{s}$  total were performed and showed that G54S perturbs the  $\alpha 2$  helix position via destabilization of the adjacent loop linked to the  $\beta 5$  sheet. This also leads to the formation of a strong H-bond between peptide target residues Leu17 and Gln66, thus restricting both the  $\alpha$ -actinin2 and LTCC C-terminal peptides to access their natural binding site and reducing in this way their binding capacity. On the basis of these observations and the adult's clinical data, we propose that ZASP<sup>G54S</sup> and presumably other ZASP PDZ domain mutations can cause HCM. To the best of our knowledge, this is the first reported ZASP PDZ domain mutation that might be linked to HCM. The integrated workflow used in this study can be applied for the identification and description of other mutations that might be related to particular diseases.



## ■ INTRODUCTION

Cypher/ZASP (*LDB3* gene), which contains a PDZ domain at its N-terminus and three LIM domains at its C-terminus, belongs to the PDZ-LIM domain protein family.<sup>1,2</sup> Cypher/ZASP is a sarcomeric protein that interacts with the Z-line proteins  $\alpha$ -actinin2, myotilin, and calsarcin and signaling molecules such as protein kinases.<sup>1,3,4</sup> Cypher plays an essential role in the maintenance of the sarcomere integrity, especially under contraction force stress.<sup>3,5,6</sup> Recently, it has been shown that ZASP is an A-kinase anchor protein (AKAP).<sup>7</sup> Thus, ZASP also appears to be a signaling center that regulates the phosphorylation of some proteins, including the L-type calcium channel (LTCC) and Cypher/ZASP itself. Similarly to enigma homologue protein (ENH), a member of the enigma family to which ZASP belongs, the PDZ domain of ZASP binds to both  $\alpha$ -actinin2 and the LTCC at their C-terminal PDZ binding motifs.<sup>7–10</sup>  $\alpha$ -Actinin2 interacts with both the PDZ and LIM domains, but only the rod is involved in binding of the ZASP LIM motif.<sup>9,10</sup> The interactions with all of the other partners described above are via solely the ZASP LIM domains. It has been demonstrated that as an AKAP, ZASP tethers protein kinase A (PKA) to the LTCC and phosphorylates Ser<sup>1928</sup> both

in vitro and in vivo.<sup>7</sup> Calcineorin (CaN), which has been reported as a phosphatase for the LTCC, also interacts with ZASP.<sup>7</sup> These findings are in line with the concept that cardiac Z-lines are signaling centers as well as important structural components of sarcomeres.<sup>11</sup>

The identification of ZASP variants associated with myopathies such as dilated cardiomyopathy (DCM), left ventricular noncompaction cardiomyopathy (LVNC), hypertrophic cardiomyopathy (HCM), and myofibrillar myopathy (zaspopathy) further demonstrates the role of ZASP in the normal function of striated muscle.<sup>4,12–17</sup> It is a feature that the LIM domains of the ENH subfamily proteins interact with protein kinase C (PKC).<sup>8</sup> For ZASP, the increased affinity to PKC caused by the mutation of Asp626 to Asn626 is associated with DCM.<sup>4</sup> Moreover, deletion of Cypher or its splice isoform in mouse hearts leads to abnormalities of certain signaling pathways.<sup>3,6</sup> To date, all of the identified disease-causing mutations are located only in ZASP's LIM domains but not in the PDZ domain. An exception is presumably the V55I

**Received:** February 21, 2014

**Published:** April 14, 2014



mutation, which has been identified in the case of LVNC but has not been confirmed confidently as a disease-causing mutation and thus is classified as a variant of unknown significance (VOUS).<sup>17</sup>

Genetic screening is a valuable tool for identification of nucleotide changes [nonsynonymous single-nucleotide polymorphisms (nsSNPs)] that cause HCM. Over 1200 mutations linked to HCM have been identified to date, found mainly in the sarcomeric proteins and to a lesser extent in the Z-disk proteins.<sup>16,18</sup> However, in certain cases the identified mutations are classified as VOUS because of a lack of more information about their particular impacts, as, for example, mutations that are rare (observed in <0.5% of the general population), sporadic, or identified in individuals without any living relatives. In such cases, the combination of gene variation data with information about regulatory functions can potentially improve the possibility of detecting pathological noncoding variants.<sup>19,20</sup>

Bioinformatics tools such as SIFT and PolyPhen-2 are excellent starting points for the identification of possible disease-causing mutations (i.e., VOUS),<sup>21,22</sup> but they use mainly machine-learning approaches and do not allow the structural or target peptide binding site changes provoked by given nsSNP to be revealed. Moreover, very recently it has been shown that the statistical difference between the HCM case and the control group was driven only for the rare nsSNP variants in the major genes (*MYH7* and *MYBPC3*) but not by the remaining minor genes included in the common genetics tests.<sup>20</sup> This has implications for many bioinformatics prediction tools such as SIFT and PolyPhen, as these tools largely rely on residue conservation, limiting the use of conservation-based tools to only two major HCM genes.<sup>20</sup>

Molecular dynamics (MD) simulations are a powerful in silico tool for both protein dynamics and structure investigation but have been only partly used in nucleotide change predictions (i.e., inadequate sampling, consideration of only local structure dynamics, etc.). They provide an important instrument to investigate at a molecular level whether some mis-sense mutations can significantly disturb the protein structure and functions, thus potentially causing a given disease. For instance, we recently demonstrated by MD simulations that the HCM-related mutations in exons 15–17 of *MYH7* can be linked to UNC-45B binding.<sup>23–25</sup>

In this study, we report the c.160G>A (Gly54Ser) nucleotide change in *LDB3* (PDZ domain of ZASP), which was identified among 50 genes in an adult with a severe form of HCM, and apply in silico MD and free energy investigations of the structural impact of G54S on ZASP itself (the apo form). In further ongoing studies, we consider in detail its impacts on the formation of the  $\alpha$ -actinin2-ZASP and LTCC-ZASP complexes. While obtaining structural insight into these experimentally unknown complexes is not a trivial task and requires many more computational and analysis resources, the MD simulations of solely ZASP<sup>G54S</sup> provide the opportunity for a relatively fast test of the hypothesis about the possible linkage of this mutation to HCM with the additional support of bioinformatics tools. The dynamics of the PDZ domains have been well-investigated by numerous experimental and in silico approaches,<sup>26</sup> and we focus here only on the G54S mutation. Our results clearly demonstrate that the G54S mutation has a significant structural and dynamical impact on the ZASP PDZ domain and that this mutation affects its binding to the target C-terminal peptides of  $\alpha$ -actinin2 and LTCC, appearing in this way as a disease-causing mutation. Discussion about how the

ZASP<sup>G54S</sup> mutant can be involved in cardiomyopathy is provided. We propose that the combination of genetics and the in silico tools applied by us may be helpful for the identification and description of other nsSNPs that might be related to particular diseases.

## METHODS

**Clinical and Genetic Screening Data.** An adult male (39 years old) was diagnosed with severe progressive obstructive HCM (septum thickness = 38 mm, LV = 73/65 mm, RV = 37/32 mm) and had a family history of sudden cardiac death. Figure S1 in the Supporting Information shows a magnetic resonance imaging (MRI) picture of the heart taken 2 years before the performed genetic screen described below. The individual had no living relatives, making the direct linkage of the identified nucleotide change to other individuals practically impossible.

A sample from this person was referred to the Emory Genetics Laboratory (<http://genetics.emory.edu/>) for genetic testing for cardiomyopathy. The cardiomyopathy panel included genes that cause HCM, DCM, LVNC, restrictive cardiomyopathy, arrhythmogenic right ventricular dysplasia/cardiomyopathy, and catecholaminergic polymorphic ventricular tachycardia. Also included were genes that cause genetic syndromes that have cardiomyopathy as a clinical feature. The following 50 genes were screened: *ABCC9*, *ACTC1*, *ACTN2*, *ANKRD1*, *BAG3*, *CASQ2*, *CAV3*, *CRYAB*, *CSRP3*, *DES*, *DMD*, *DSC2*, *DSG2*, *DSP*, *DTNA*, *EMD*, *GAA*, *GLA*, *JPH2*, *JUP*, *LAMA4*, *LAMP2*, *LDB3*, *LMNA*, *MTTG*, *MTTI*, *MTTK*, *MYBPC3*, *MYH6*, *MYH7*, *MYL2*, *MYL3*, *MYOZ2*, *NEXN*, *PKP2*, *PLN*, *PRKAG2*, *RBM20*, *RYR2*, *SGCD*, *TAZ*, *TCAP*, *TMEM43*, *TNNC1*, *TNNI3*, *TNNT2*, *TPM1*, *TTN*, *TTR*, and *VCL*.

Polymerase chain reaction (PCR) amplification of all of the coding exons within the cardiomyopathy-associated genes tested was performed on the individual's genomic DNA. Exon 153 of the *TTN* gene could not be analyzed because of the complexity of the sequence in that region. Direct sequencing of the amplification products was performed using next-generation short base pair read sequencing. For exons with inadequate coverage by next-generation sequencing, the Sanger sequencing method was used to sequence the PCR products in the forward and reverse directions. Intronic changes greater than 10 nucleotides from the exon–intron boundaries were not analyzed. In some cases, because of the complexity of the sequence, not all of the nucleotide changes in the flanking intron sequence could be analyzed. Nucleotide changes were evaluated by their reported frequency, and when they had a population frequency greater than the expected prevalence in the general population, they were considered to be benign polymorphisms. A detailed clinical report and the genetic test data of the HCM-diagnosed individual are available upon request.

The initial conclusion about the possibility that the identified c.160G>A nucleotide change in the *LDB3* gene is HCM-linked was first evaluated on its frequency in the general population using the ESP (ESP6500SI-V2 release)<sup>27</sup> and 1000K<sup>28</sup> genetic databases. The latter approach has been strongly recommended for newly registered likely-disease-causing nsSNPs.<sup>29</sup>

**Bioinformatics Prediction of Functional Consequences.** To prioritize further investigations, the potential consequences of the nonsynonymous variant c.160G>A of

LDB3 were predicted by means of the four different bioinformatics methods described below:

(1) The type of amino acid mutation was categorized on the basis of nonsynonymous Grantham values, which range from 5 to 215 and provide a measure of chemical similarity. Grantham scores of <50 are usually classified as nonsynonymous conservative, 51–100 as moderately conservative, 101–150 as moderately radical, and >151 as radical.<sup>30</sup>

(2) SIFT is an algorithm for predicting functional consequences of amino acid substitutions that assigns scores by considering alignments of orthologous sequences.<sup>21</sup> SIFT is a multistep procedure that for a given protein sequence (i) searches for similar sequences, (ii) chooses closely related sequences that may share similar function, (iii) obtains the multiple alignment of the chosen sequences, and (iv) calculates normalized probabilities for all possible substitutions at each position from the alignment. SIFT scores range from 0 to 1: scores of <0.05 indicate variant sites in codons for evolutionarily conserved amino acids that are predicted to be deleterious, whereas scores of ≥0.05 are more likely to be tolerated.<sup>21</sup>

(3) PolyPhen-2 uses empirically derived rules and computes the absolute value of the difference between the profile scores for the two variants to predict the likelihood that an nsSNP affects the protein function or structure.<sup>22</sup> PolyPhen-2 performs multiple alignments with homologous sequences using BLAST and calculates a position-specific independent count (PSIC) score for each position of the sequence in the profile matrix. The PSIC score is given by the log-likelihood that the given amino acid occurs at a particular position.<sup>31</sup> PolyPhen-2 then computes the absolute value of the difference between the profile scores of the wild-type and variant amino acid residues for a specific position ( $d\text{Score} = \text{Score1} - \text{Score2}$ ), which corresponds approximately to the log-likelihood of substituting the wild-type amino acid for the mutant amino acid. It also annotates the substitution site (e.g., active or binding) and maps the substitution site onto a known three-dimensional (3D) protein structure to indicate whether the substitution will affect any important feature of the protein. Finally, it checks for any contact within the functional sites, such as contacts with ligands, interactions between subunits of the protein, and contacts with “critical” residues.<sup>22</sup> The prediction of the functional effect is calculated as the naïve Bayes posterior probability, and the qualitative prediction is based on cutoffs of the score. The maximal “damaging” score of PolyPhen-2 is equal to 1.

(4) FOLDX 3.0 utilizes the 3D protein structure and an empirical potential with different energy terms to predict the difference in the Gibbs free energies of unfolding ( $\Delta\Delta G$ ) for the wild-type (WT) and mutant proteins [ $\Delta\Delta G = \Delta G(\text{mutant}) - \Delta G(\text{WT})$ ].<sup>32</sup> Mutations leading to changes of >1 kcal/mol in  $\Delta\Delta G$  are considered destabilizing, and those leading to changes of <−1 kcal/mol in  $\Delta\Delta G$  are considered stabilizing. The range  $1 \text{ kcal/mol} \geq \Delta\Delta G \geq -1 \text{ kcal/mol}$  is considered neutral.

The assessment of mutations by each program was carried out with default settings.

**Classical Molecular Dynamics Simulations.** A series of classical molecular dynamics (cMD) simulations were employed to guarantee the reliability of the reported results. In this way, the conformational space can be better sampled and the possibility of being in a single local energy minimum during the whole simulation time can be avoided. Hence, in a comparison of two similar structures, as in the case of a single-

point mutation, using only one simulation per protein does not guarantee that the observed differences are really linked to this point mutation. There might be another local energy minimum that could be present in the wild-type protein too. If one wants to distinguish the real differences provoked by a single-point mutation from the conformations present on the free energy landscape of the studied wild-type protein, a sufficient number of individual cMD simulations should be performed. cMD is a statistical approach, and one can confidently conclude that certain conformational changes are related to the point mutation if they are repeatedly observed in the mutant form and not in the wild-type protein. Thus, to sample the ZASP<sup>GS4S</sup> conformational space better, a number of independent simulations were executed.

Five independent cMD runs with lengths of 100–200 ns were initially performed on both the ZASP<sup>WT</sup> and ZASP<sup>GS4S</sup> proteins, followed by two additional runs of 300 and 400 ns using as a start the cMD structures obtained in the initial runs. Details about these cMD simulations are collected in Table S1 in the Supporting Information. The Protein Data Bank structure (PDB ID 1RGW) was used to obtain the starting structure of the human ZASP<sup>WT</sup> protein, whereas the final averaged structures were retrieved from the last 20 ns of the simulation time.

The system was solvated in a truncated octahedron with edges no closer than 10 Å to any protein atom and neutralized by counterions. The solvent was represented by the TIP3P standard model. All simulations were performed with the Amber 12 package using the AMBER ff12SB force field.<sup>33–35</sup> The systems were energy-minimized in two steps. First, only the water molecules and ions were minimized for 6000 steps while keeping the protein structure restricted by weak harmonic constrains of 2 kcal mol<sup>−1</sup> Å<sup>−2</sup>. Second, a 6000 step minimization with the conjugate gradient method (convergence criterion of 0.1 kcal mol<sup>−1</sup> Å<sup>−2</sup>) on the whole system was performed. Furthermore, the simulated systems were gradually heated from 0 to 310 K for 50 ps (NTV ensemble) and equilibrated for 3 ns (NPT ensemble). The production runs were performed at 310 K in an NPT ensemble. Temperature regulation was done using a Langevin thermostat with collision frequency of 2 ps<sup>−1</sup>. The time step of the simulations was 2 fs with a nonbonded cutoff of 9 Å using the SHAKE algorithm<sup>36</sup> and the particle-mesh Ewald method.<sup>37</sup> All root-mean-square fluctuation (RMSF) calculations were based on the overall production run trajectory. Calculations of the residue contacts between the refined complexes, H-bonds, and visualizations were obtained using the Maestro module of the Schrödinger software.<sup>38</sup>

**Accelerated Molecular Dynamics Simulations.** The accelerated molecular dynamics (aMD) simulations provide the possibility to sample the conformational space much better and to detect the local energy minima that remain hidden in the cMD calculations.<sup>39,40</sup> aMD does not represent the real protein dynamics but is useful to investigate whether a protein conformation is present on the free energy landscape and how the latter changes in the ZASP mutant form. Moreover, the aMD simulations typically boost the sampling by about 2000 times relative to cMD.<sup>34</sup> Thus, one can consider that the sampling performed by a 50 ns aMD trajectory might be equal to that of hundreds of nanoseconds of cMD simulation. aMD modifies the energy landscape by adding a boost potential  $\Delta V(r)$  to the original potential energy surface when  $V(r)$  is below a predefined energy level  $E$ :

$$\Delta V(r) = \begin{cases} 0 & V(r) \geq E \\ \frac{[E - V(r)]^2}{\alpha + [E - V(r)]} & V(r) < E \end{cases} \quad (1)$$

In principle, this approach also allows the correct canonical average of an observable calculated from configurations sampled on the modified potential energy surface to be fully recovered from the aMD simulations.<sup>34</sup>

All of the aMD calculations were performed using the Amber 12 molecular modeling package.<sup>33–35</sup> In order to simultaneously enhance the sampling of internal and diffusive degrees of freedom, a dual-boosting approach based on separate dihedral and total boost potentials was employed.<sup>34,39</sup> The selections of the boost parameters  $E$  and  $\alpha$  for the dihedral boost and the total boost were based on the corresponding average dihedral energy and total potential energy obtained from the above-performed cMD equilibration runs, respectively. The dihedral boost parameter,  $E_d$ , was set equal to the average dihedral energy obtained from the cMD simulation plus  $N_{sr} \times 3.5$  kcal/mol, where  $N_{sr}$  is the number of solute residues; the  $\alpha_d$  parameter was then set equal to  $E_d/5$ . For the total boost parameter,  $E_{tot}$ , the value was set to be equal to  $0.16N_{tot}$  plus the average total potential energy obtained from the cMD simulation, where  $N_{tot}$  is the total number of atoms;  $\alpha_{tot}$  was simply set equal to  $0.16N_{tot}$ .

Two 50 ns independent aMD runs were performed for ZASP<sup>WT</sup> and for ZASP<sup>G54S</sup>. However, to adjust the boost parameters, initially a set of four 50 ns aMD simulations were performed. The mutant protein was also submitted to an additional 300 ns longer aMD simulation starting from the cMD2 structure.

When we increased the value of  $E_d$  by adding multiples of  $\alpha_d$ , we observed that the structures become disrupted and did not have any physical sense. Thus, the minimal  $E_d$  boost as described above was chosen. The aMD simulation was carried out using the exact same conditions as described for the above cMD simulation. Several two-dimensional free energy profiles were reweighted using the procedure described previously<sup>34</sup> as applied to the principal component analysis (PCA) plots.

**Free Energy Calculations.** Free energy calculations were performed by the molecular mechanics Poisson–Boltzmann surface area (MM-PBSA) method using the MMPBSA.py script included in the AmberTools 13 package.<sup>33,41</sup> The analysis was based on the last 20 ns of all of the cMD trajectories. In order to evaluate the individual contributions of the selected residues and/or structural elements, a decomposition of the free energy contributions approach was employed. A pairwise per-residue-basis decomposition for the selected protein residues was chosen. Pairwise decomposition calculates the interaction energy between all pairs of residues in the system. The MMPBSA.py script was initially developed for calculation of ligand–receptor interactions and currently requires specification of a ligand. Thus, the protein was virtually divided into two parts: a ligand that consists of the  $\beta$ S– $\alpha$ 2 loop (residues 54–60) and a receptor for the remaining residues. However, all of the calculations were based only on summation of the pairwise free energies between the residues of interest taken from the output file. For instance, to access the interactions between the  $\alpha$ 2 helix and the  $\beta$ S– $\alpha$ 2 loop, we calculated all of the pairwise free energies between residues involved in these structural elements. All of the decomposed energies were calculated by the MM-PBSA method.

The MM-PBSA is a widely used approach for free energy calculations, and a detailed description of the methodology can be found elsewhere.<sup>23,42</sup> Shortly, for each frame extracted from the cMD trajectory (a 50 ps interval was set here), the enthalpic free energy was calculated as follows:

$$\Delta G_{bind} = \Delta G_{gas} + \Delta G_{solv} - T\Delta S \quad (2)$$

$$\Delta G_{gas} = \Delta G_{ele} + \Delta G_{vdW} \quad (3)$$

$$\Delta G_{solv} = \Delta G_{PB} + \Delta G_{nonpolar} \quad (4)$$

$$\Delta G_{nonpolar} = \gamma A + b \quad (5)$$

The free energy was obtained as an average over all frames used. It includes van der Waals (vdW) contributions, electrostatic contributions, and polar and nonpolar contributions to the solvation free energy ( $\Delta G_{solv}$ ). The gas-phase free energy ( $\Delta G_{gas}$ ) was obtained using the sander module of Amber 12, and the estimation of  $\Delta G_{PB}$  was conducted by MMPBSA.py.  $\Delta G_{nonpolar}$  was determined from eq 5, in which  $A$  is the solvent-accessible surface area, estimated using the Molsurf program (a part of the Amber 12 suite of programs) with a solvent probe radius of 1.4 Å, and  $\gamma$  and  $b$  are empirical constants set to 0.0072 kcal mol<sup>-1</sup> Å<sup>-2</sup> and 0.92 kcal/mol, respectively. The entropy term ( $T\Delta S$ ) was neglected in these calculations.

As far as decomposition is concerned, a reasonable way involved splitting the electrostatic contribution to the free energy ( $\Delta G_{PB}$ ) into two parts, a self/desolvation energy and an interaction/pairwise energy. The self-energy is the value of  $\Delta G_{PB}$  when only the residue of interest is charged while all other residues remain neutral; the interaction energy is the charging energy of the residue in the field of all other charged residues. Thus, the procedure applied here involves two numerical solutions of the Poisson–Boltzmann equation with differently charged states for each residue of interest.

**Correlation Analysis.** The correlation analysis of the MD trajectories is a useful approach for studying the protein dynamics. Cross-correlation maps of the residues' motion were used to identify the regions that were moving in or out of phase during the simulations. Thus, this method can provide information about the impact of the G54S mutation on the protein dynamics and specify which structural elements are involved in the structural changes and what is their role. The elements  $b_{ij}$  of the correlation matrix  $B$  were obtained from  $\mathbf{r}_i$  and  $\mathbf{r}_j$ , the position vectors of residues  $i$  and  $j$ , as

$$b_{ij} = \frac{\langle (\mathbf{r}_i - \langle \mathbf{r}_i \rangle)(\mathbf{r}_j - \langle \mathbf{r}_j \rangle) \rangle}{\sqrt{\langle (\mathbf{r}_i^2) - \langle \mathbf{r}_i \rangle^2 \rangle \langle (\mathbf{r}_j^2) - \langle \mathbf{r}_j \rangle^2 \rangle}} \quad (6)$$

Only the C $\alpha$  displacements were considered during the calculations, which were performed using the P traj module of the AmberTools 13 program.<sup>33,43</sup> All of the frames of the MD trajectories were aligned on the preequilibrated structure (the input for the production run) with an interval of 50 ps. The analysis was based on all of the obtained MD trajectories. The value of  $b_{ij}$  can vary from  $-1$  (completely anticorrelated motion) to  $+1$  (completely correlated motion). It should be noted that with the above formula it is impossible to detect orthogonal correlative motion. The entire cMD trajectories from all of the performed runs were included in these calculations.

**Principal Component Analysis.** PCA analysis is another helpful tool for studying differences in the protein dynamics, in particular those of the substructural elements of interest. In short, PCA is a dimensional reduction technique that allows the isolation of the most significant conformational differences among a set of structures. In the MD analysis these structures were extracted as snapshots from the aligned MD trajectory, and then the correlation matrix was calculated and diagonalized, providing an orthogonal set of eigenvectors representing linearly independent modes of conformational changes. These are the principal components (PCs). The eigenvalue associated with each PC is a measure of the variance in the original data set explained by that component. In order to identify the conformational changes provoked by the G54S mutation and particularly those in the  $\alpha 2$  helix, the entire cMD trajectories from all of the performed runs were included in these calculations. In some cases only the last 20–40 ns of the simulations were employed (e.g., for the visualization of the PC1 projection on the protein structures, only the last but well-equilibrated portion of the cMD trajectories was used); these exceptions are noted in the text. In this work, the PCAs were performed on the  $C\alpha$  coordinates using the P traj and C traj modules of the AmberTools 13 package, and the results are presented as heat maps of the first two PCs (PC1 and PC2).<sup>33</sup> A heat map is a relative free energy surface with 0 as the most stable state, a bin size of 1, and values calculated as  $-k_B T \ln(\text{bin}/\text{max})$ , where max is the most-populated bin. Projections of the motion corresponding to PC1 onto the protein structures were calculated using the Prody software.<sup>44</sup>

## RESULTS

**Genetic Data and Bioinformatics Analyses.** The c.160G>A (Gly54Ser) nucleotide change in the *LDB3* gene has not been reported to date in individuals with cardiomyopathy. The same variant has been reported in the general population; however, there was insufficient information to draw a conclusion about its clinical significance. Thus, the c.160G>A (p.G54S) nucleotide change in the *LDB3* gene has been classified as VOUS. However, this result must be interpreted in the context of the individual's clinical features.

Many nucleotide changes contributing to diseases are likely to be segregated at low frequency.<sup>29,44</sup> Thus, it has been recommended that the variant frequency should be considered when using the resource to identify pathological candidates.<sup>29</sup> The c.160G>A nucleotide change in the *LDB3* gene (G54S in ZASP) reported here is very rare and has been observed in the general populations with a frequency of 0.01% (in just one out of 6503 studied individuals) according to the ESP database (ESP6500SI-V2 release).<sup>27</sup> This mutation was also found by the 1000K Gene Project<sup>28</sup> with a frequency of 0.09% in the selected population of 1092 individuals.

The residue Gly54 is one of the highly conserved residues in the ZASP PDZ domain, and the G54S mutation could be classified as nonsynonymous conservative. A GERP score<sup>45</sup> of 5.68 (with 6.17 being the most conserved) and a Grantham score<sup>46</sup> of 56 (possible range from 5 to 215) were obtained. Thus, it is not unexpected that SIFT estimated this mutation to have the highest damaging score (equal to zero). The PolyPhen-2 bioinformatics tool classified G54S with the maximum damaging score of 1 as well. The free energy change of  $\Delta\Delta G = +3.61$  kcal/mol calculated by FOLDX3.0 clearly demonstrated that the mutation could be considered as destabilizing. To validate this result, we also estimated the

energy changes of some known ZASP mutations that affect the  $\alpha$ -actinin2–ZASP binding. The F15A, H62A, L76K, L78K, and L80K mutants gave  $\Delta\Delta G$  values of 6.12, −0.17, 3.99, 5.11, and 3.50 kcal/mol, respectively. This agrees with the experimental results: while F15A completely abolished the formation of the  $\alpha$ -actinin2–ZASP complex and L76K, L78K, and L80K significantly reduced the binding, the mutation of His62 to Ala had only a marginal effect.<sup>4,5</sup> All of these data indicate that the G54S mutation identified in *LDB3* is a promising indicator for a nucleotide change possibly associated with HCM in the studied individual.

**Comparison between Experimental Data and the cMD Results for ZASP<sup>WT</sup>.** To validate our computational results, we first compared the structures of ZASP<sup>WT</sup> obtained by MD simulations to the experimental ZASP<sup>WT</sup> structures obtained by NMR techniques.<sup>10</sup> In total, five independent cMD and two aMD runs were performed. The average MD structure of ZASP<sup>WT</sup> overlapped well with the NMR structures: the root-mean-square deviation (RMSD) of the backbone atoms was 1.4 Å (Figure S2 in the Supporting Information). A slight shift was recorded in the  $\beta 2$  sheet (residues 15–19). Furthermore, we compared also the RMSF values between the 20 NMR structures and those from the MD simulations. Most of the fluctuating regions were in particular identical, and both the NMR and cMD techniques identified the residues at positions 10, 24, 35, 53, 58, and 73 to be highly flexible in ZASP<sup>WT</sup> (Figure S3A in the Supporting Information). The maximum difference in the fluctuation amplitudes was on the order of only 0.5–0.7 Å. Finally, we used a correlation analysis to check whether most of the collective motions observed by NMR were also represented in the MD simulations. As shown in Figure 1A and Figure S4 in the Supporting Information, most of the correlative motions detected by NMR techniques were also detected by the MD approach. On the basis of these results, we concluded that there was a good agreement between the correlative motions of the protein structural elements observed experimentally and in silico. An exception was the degree of the observed correlation. This could likely be due to the fact that the number of MD frames was much larger than the number obtained by NMR measurements and that the less sampled systems exhibit stronger correlations between much of the proteins.<sup>47</sup> Thus, the above comparison between the experimental and in silico results for ZASP<sup>WT</sup> provides good evidence that the performed simulations can provide valuable structural and dynamical information about the impact of the G54S mutation on the human ZASP protein.

**Structural Changes Observed in the ZASP<sup>G54S</sup> Mutant.** Despite the good general overlap between ZASP<sup>WT</sup> and ZASP<sup>G54S</sup> (RMSD of 1.3 Å between the backbone atoms) after the fast equilibration steps (Figure S3B in the Supporting Information), a significant discrepancy was observed in the position and fluctuation of the binding site structural elements. This fact deserves attention because of the possible influence on the C-terminal peptide binding of target proteins such as  $\alpha$ -actinin2 and the LTCC. First, the loop between the  $\beta 5$  and  $\alpha 2$  elements (called here the  $\beta 5$ – $\alpha 2$  loop) was transformed into a new, more stable helixlike structure in ZASP<sup>G54S</sup> (Figure 2). Considering that the  $\beta 5$  sheet accommodates the G54S mutation, we assumed that this structural perturbation was provoked by the mutation itself. This is also seen well from the displacement of the  $C\alpha$  atom of residue 54 by 1.34 Å in the mutated form relative to the wild type. Furthermore, a large displacement of the  $\alpha 2$  helix position was observed. The

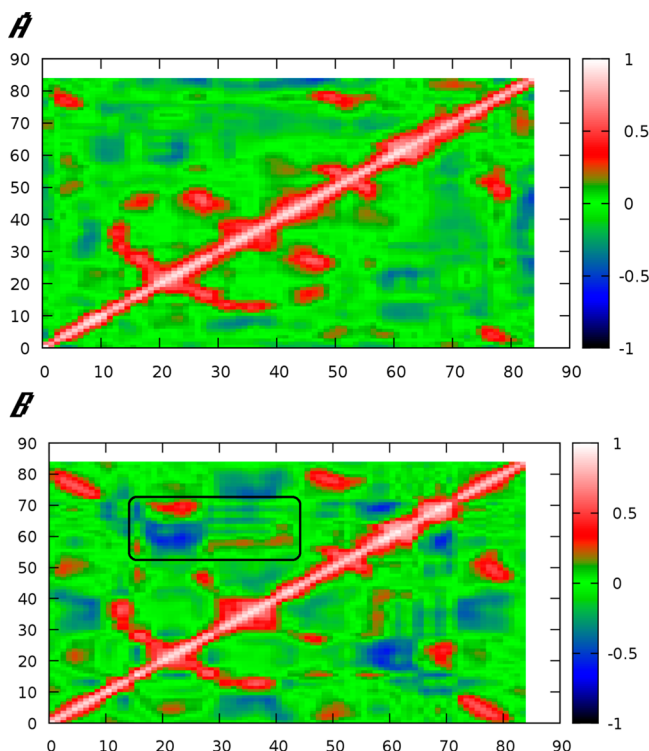


**Figure 1.** Observed correlations between the residues' motion in (A) ZASP<sup>WT</sup> and (B) ZASP<sup>G54S</sup>. The red areas mark the residues with correlative motion (i.e., simultaneous motions in the same direction with a positive correlation coefficient), whereas the blue ones show those with anticorelative motion (i.e., motion in opposite directions with a negative correlation coefficient). The green areas are neutral. The black contour indicates the discussed differences observed in ZASP<sup>G54S</sup>.

averaged structures showed that the bottom end of this helix is closer to the  $\beta_2$  sheet in the wild type than in the mutant. The distances between the C $\alpha$  atoms of Gly20 and Thr61 averaged over all runs were  $4.9 \pm 0.5$  and  $6.9 \pm 1.0$  Å in ZASP<sup>WT</sup> and ZASP<sup>G54S</sup>, respectively. In the  $\alpha_2$  helix of ZASP<sup>G54S</sup>, the average distance between the above residues was  $7.7 \pm 1.2$  Å during 64% of the simulation runs, while distances above 6.5 Å were present in only 38% of the cMD runs for the wild type. Finally, a difference in the position of the  $\beta_2$  sheet that was slight but reproduced in all of the cMD and aMD runs was clearly visible in ZASP<sup>G54S</sup> (Figure 2A) and is presumably due to the changes recorded in the  $\alpha_2$  helix position.

The most striking difference between ZASP<sup>WT</sup> and ZASP<sup>G54S</sup> structures was the formation of a H-bond between the side chain of Gln66 in the  $\alpha_2$  helix and the backbone of Leu17 in the  $\beta_2$  sheet (Figure 3). It was present in the mutant in 67.6–80.5% of all of the individual cMD runs but observed briefly (24.4–34.4%) in ZASP<sup>WT</sup>. A mean value of 75.4% for the lifespan of the Leu17–Gln66 H-bond in ZASP<sup>G54S</sup> was recorded in all of the performed simulations. The formation of this H-bond was favored in the mutant because of the more frequent opening of the binding site provoked by the  $\alpha_2$  helix displacement, which exposes the C=O group of Gln66 to the backbone N atom of Leu17. In the wild type this is restricted because of the shorter distance between the backbones of the  $\alpha_2$  helix and the  $\beta_2$  sheet. Arg16 was also displaced toward the  $\alpha_2$  helix by an average distance of 0.9 Å in the mutant relative to ZASP<sup>WT</sup>. Moreover, the hydrophobic core residues Val49

and Ile52 and the  $\beta_2$  sheet's Leu17 stand in good contact (see Figure S5 in the Supporting Information), being positioned almost in a rectangular triangle with a distance of 4 Å between the closest heavy atoms, suggesting that Ile52 can perturb the binding site geometry too.

To investigate whether these observations are not just an effect of the mutant adaptation but represent instead the real dynamical behavior of the protein, a new 400 ns cMD simulation was performed starting from the structure obtained after the 120 ns simulation (run cMD4; see Table S1 in the Supporting Information). The results confirmed that the observed strong H-bond between Leu17 and Gln66 was stable during 71.3% of the simulation time, and an average distance of  $2.85 \pm 0.17$  Å between the acceptor and donor atoms was measured. The observed fluctuations in the bottom of the  $\alpha_2$  helix (Figure S3 in the Supporting Information) were also confirmed. The average distance between the C $\alpha$  atoms of Gly20 and Thr61 was  $7.6 \pm 1.3$  Å, and distances of more than 6.5 Å were recorded during 80.6% of the simulation time, demonstrating the stable  $\alpha_2$  helix displacement in ZASP<sup>G54S</sup>. The bottom of the  $\alpha_2$  helix was shifted by 5° in a direction opposite to the  $\beta_2$  sheet. In the 300 ns individual run for ZASP<sup>WT</sup>, the lifespan of the H-bond increased but took place in only 43% of the simulation time, and more frequent fluctuations were observed. Thus, these simulations confirmed once more the above-suggested structural effect of the single-point mutation on the dynamic behavior of the protein.

In summary, the above comparison of the simulated ZASP<sup>WT</sup> and ZASP<sup>G54S</sup> structures suggests that G54S significantly perturbs the  $\beta_5$ – $\alpha_2$  loop, which reflects on the position of the adjacent  $\alpha_2$  helix shifting in this way the  $\beta_2$  sheet position and favoring the formation of the Leu17–Gln66 H-bond. This clearly shows that the G54S mutation changes the peptide binding pocket geometry.

The above observations were first confirmed by a simple RSMF analysis averaged over all of the simulation runs. This confirmed that the  $\alpha_2$  helix and in particular residues 60–64 are more flexible in ZASP<sup>G54S</sup> than ZASP<sup>WT</sup> (Figure S3 in the Supporting Information). Fluctuations in the neighboring  $\beta_2$  sheet were also well-expressed. A significant difference in fluctuations was recorded for residues 30–45 and in particular residues 40–45, which were much more flexible in ZASP<sup>G54S</sup>. These residues constitute the portion between the  $\alpha_1$  helix and the central  $\beta_4$  sheet. It is noteworthy that the  $\beta_4$  sheet is a part of the hydrophobic core of the PDZ domain and comprises the Val49 and Ile52 residues. The observed larger RMSFs in the 40–45 region in ZASP<sup>G54S</sup> are likely due to the changes provoked in Leu17 too. This residue shifts its position in the mutant and perturbs the neighboring Ile29, which in turn makes a close contact with the region and in particular with Leu43. Almost an identical result was observed in the RMSF data from the 400 ns cMD simulation, proving that the detected fluctuations are due to the changes in the dynamical behavior of the protein as a result of its mutation.

Furthermore, we investigated whether the G54S mutation could destabilize the ZASP structure, as was predicted above by FOLDX3.0. The average of the potential energies of all the performed cMD runs had a value of  $-40\,699 \pm 100$  kcal/mol for the mutant, whereas for the wild type the value was  $-41\,150 \pm 100$  kcal/mol, thus implying that ZASP<sup>G54S</sup> is more unstable than the wild type. To trace out how the energies changed during the simulation time, we split the mutant simulation cMD4 run (total length of 120 ns) into three portions and

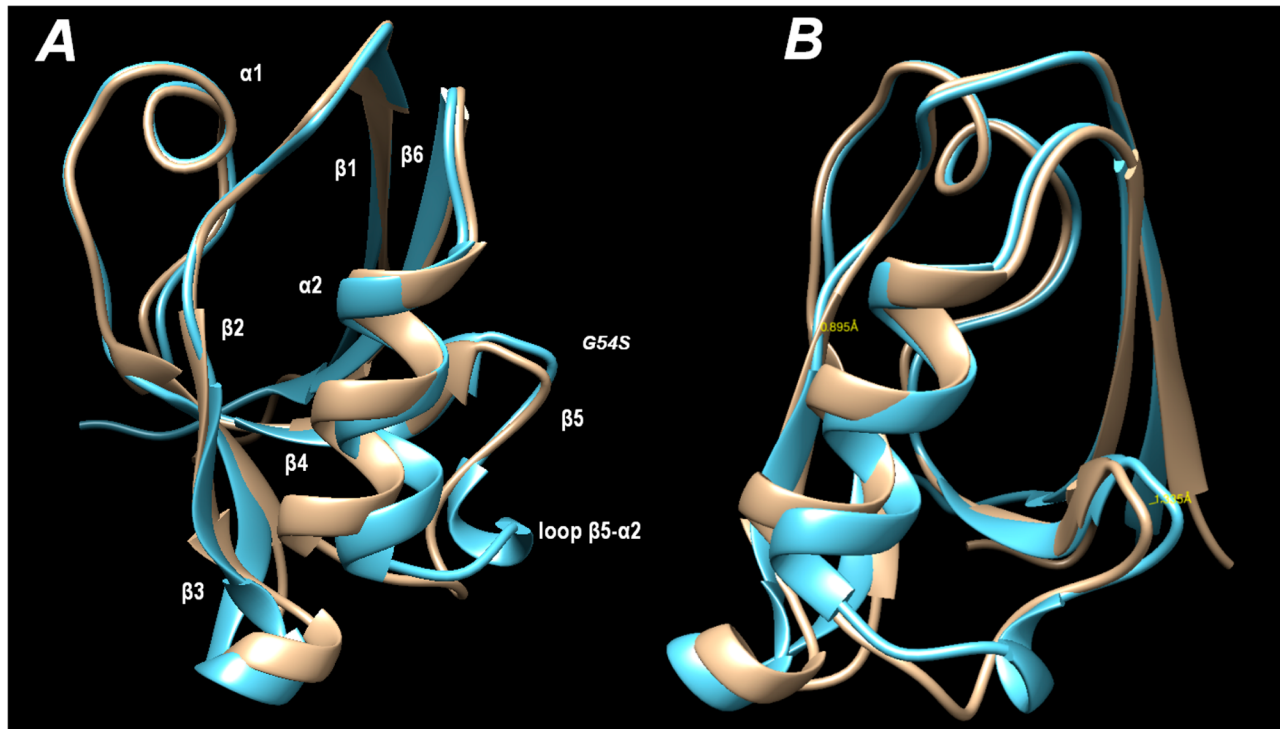


**Figure 2.** Average structures obtained from the last 20 ns of all cMD runs of ZASP<sup>WT</sup> (in wheat color) and ZASP<sup>G54S</sup> (in sky-blue color). (A) Front view of the protein with the C-terminal target peptide binding site (between the  $\alpha 2$  helix and the  $\beta 5$  sheet), with the structural elements assigned. (B) Side view (rotated 90° from A). The distances between the  $C\alpha$  atoms of the residues at positions 54 and 17 are also shown.

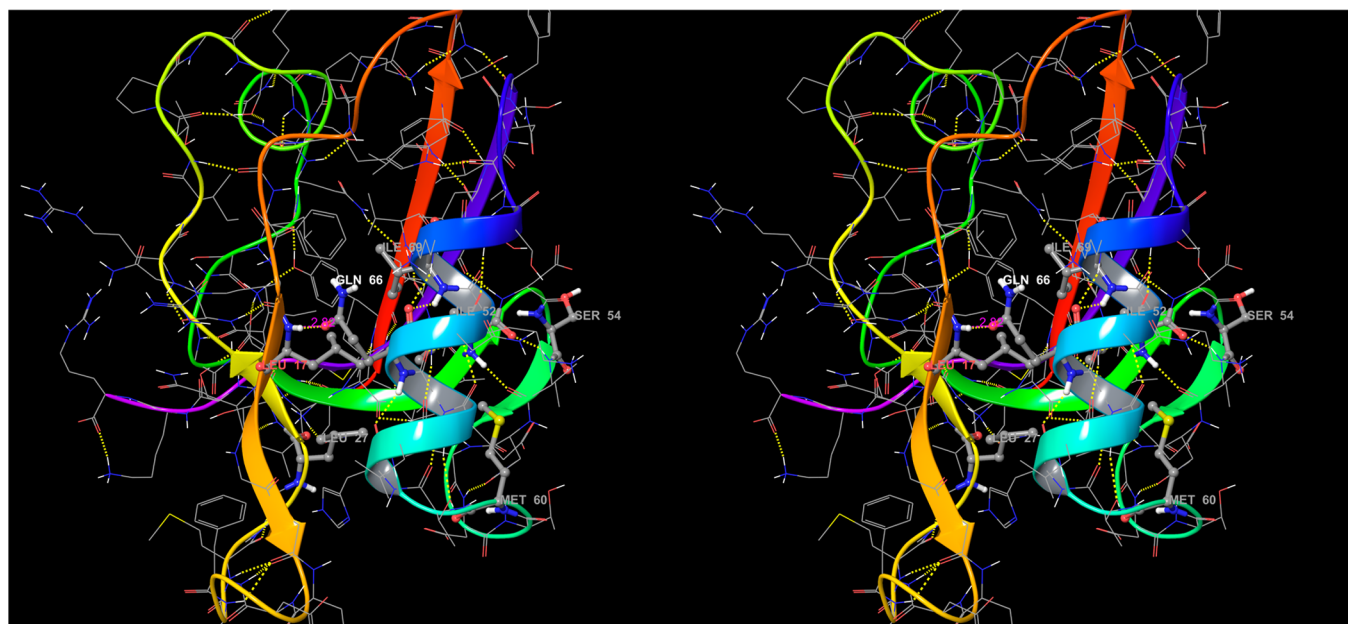


**Figure 3.** Stereo view of the ZASP<sup>G54S</sup> mutant. The H-bond between Leu17 and Gln66 and the corresponding distance between the donor and acceptor atoms are noted. The additionally observed H-bond networks are also shown as dashed lines.

extracted the averaged values within the 40 ns intervals. As a result, we obtained a difference of 10.2 kcal/mol between the first and second intervals and a 7.1 kcal/mol difference between the second and third intervals. The total deviations between individual simulations either on the mutant or the wild type were in the range of only 5–10 kcal/mol. These results imply that most likely the G54S mutation has a destabilizing effect on the ZASP structure.

**Differences between ZASP<sup>WT</sup> and ZASP<sup>G54S</sup> Protein Dynamics: Correlation, PCA, and aMD Analyses.** The correlation analysis displayed differences in the protein dynamics of ZASP<sup>WT</sup> (Figure 1A) and ZASP<sup>G54S</sup> (Figure 1B). The most notable was the anticorrelative motion (i.e., simultaneous movement in different directions) of the whole  $\beta 5-\alpha 2$  helix segment, including the G54S mutation, and the  $\beta 2$  sheet. This observation was not recorded for ZASP<sup>WT</sup> and

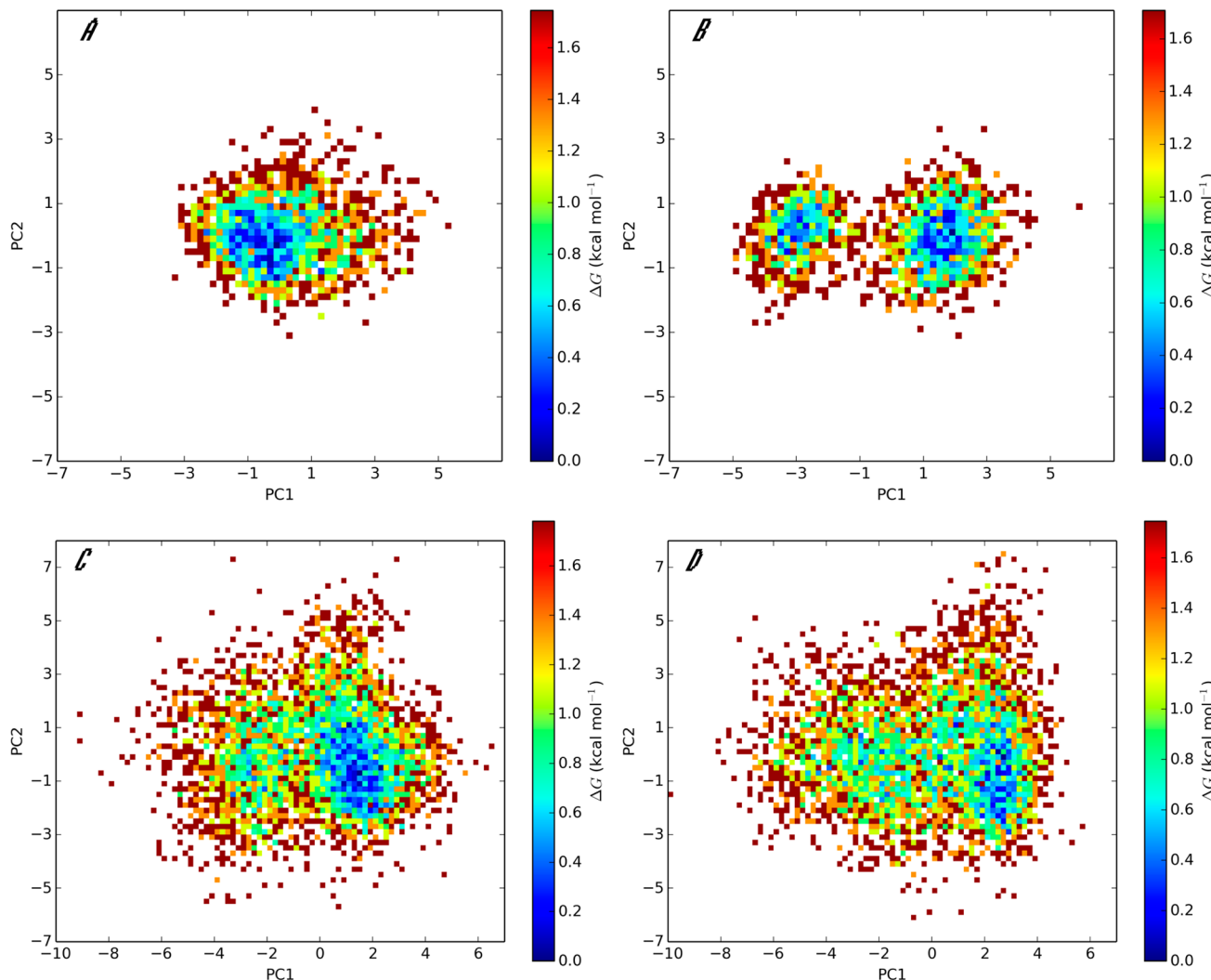


**Figure 4.** PCA of the  $\alpha_2$  helix motion (PC1 vs PC2), presented as heat maps of free energy (in kcal/mol), observed by cMD in (A) ZASP<sup>WT</sup> and (B) in ZASPG<sup>54S</sup> and by reweighted aMD in (C) ZASP<sup>WT</sup> and (D) in ZASPG<sup>54S</sup>. It should be noted that the aMD results confirm the presence of two likely conformational states in both ZASP<sup>WT</sup> and ZASPG<sup>54S</sup> that according to the cMD results are differently occupied in the wild type and mutant.

clearly demonstrated that the changes in the target peptide binding site were provoked by the G54S mutation and in particular by the changes in the  $\beta_5-\alpha_2$  loop. Moreover, part of the  $\beta_5-\alpha_2$  loop had correlative motions with the above-mentioned residues 40–45 in ZASPG<sup>54S</sup>, which was not observed in the wild-type protein. This phenomenon was much more expressed in the aMD simulations (Figure S7 in the Supporting Information) and confirmed that the changes in this segment were provoked by the G54S mutation and also by the transformation of the  $\beta_5-\alpha_2$  loop. The two independent aMD runs on both the wild type and the mutant revealed that a new helixlike structural element between residues 40 and 45 appeared in ZASPG<sup>54S</sup> (Figure S8 in the Supporting Information). The aMD runs also confirmed the disposition of the  $\alpha_2$  helix. While the transformation of the latter was relatively fast, the structural change of structural elements adjacent to the  $\alpha_1$  helix (40–45 region) apparently required much more time. It should be also noted that Ile69 had correlative motions with Met25, which might be an indication that additional perturbations via the Asp53–Ile62 pair affecting the  $\beta_2$  and  $\beta_3$  sheets are also possible (i.e., Leu27–Ile17 interactions). Moreover, the correlative motion of the Gly54–Leu27 pair and the anticorrelative motion of the Pro34–Trp13

pair show that changes in the  $\alpha$ -actinin binding site are also possible via the  $\beta_3$  sheet. Thus, the G54S mutation affects not only the binding site but also the dynamics of the PDZ ZASP domain itself and of the other elements that are indirectly linked to the peptide binding.

PCA of the motion of the  $\alpha_2$  helix showed that in ZASPG<sup>54S</sup> there were two distinguished clusters that corresponded to the initial state and the state displaced by the G54S mutation. Conversely, in ZASP<sup>WT</sup> there was only one cluster (compare panels A and B in Figure 4). The shifted  $\alpha_2$  helix conformation was poorly sampled in the wild type, whereas in the mutant the cluster representing the changed  $\alpha_2$  helix position was more populated, in agreement with the above measured changes in the distances. These findings confirm that the observed changes are linked to differences in the protein dynamics provoked by the destabilization effect of the mutation and that adequate sampling of the identified conformational state (i.e., the energy minimum) takes at least 70–120 ns.

To check whether the above-described conformation really exists in the free energy landscapes, we further performed the same analysis on the reweighted aMD runs (Figure 4C,D). Indeed, the aMD sampled the conformational space much better, and two identical clusters were present in both ZASP<sup>WT</sup>

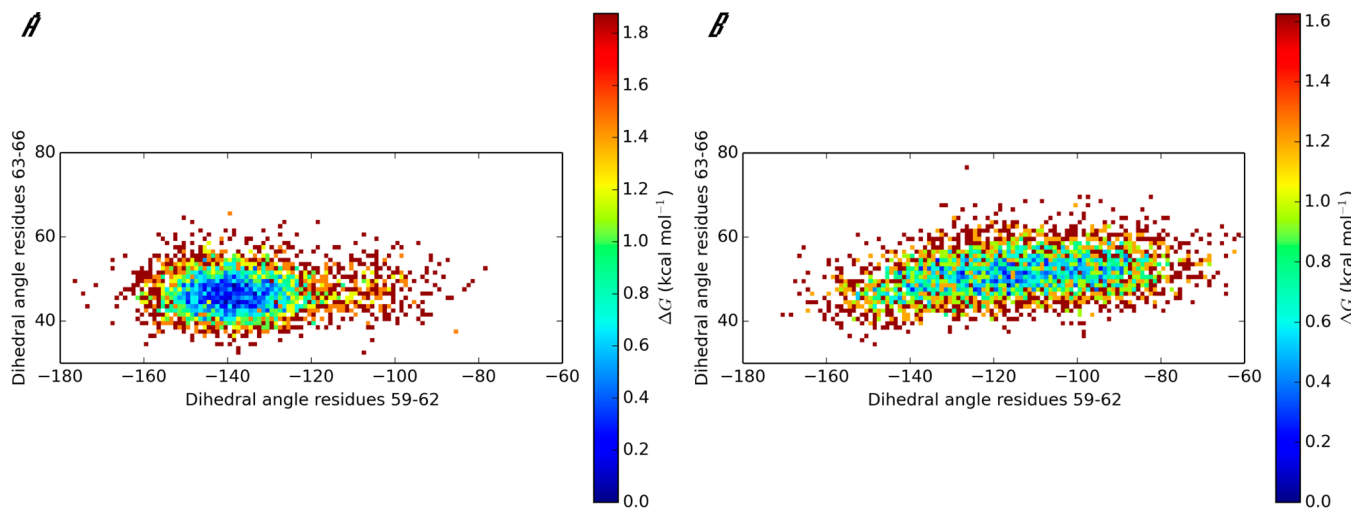


**Figure 5.** Plots of the virtual dihedral angle between the C $\alpha$  atoms of residues 63–66 versus that of residues 59–62, presented as heat maps of free energy (kcal/mol), for (A) ZASP<sup>WT</sup> and (B) ZASPGS4S.

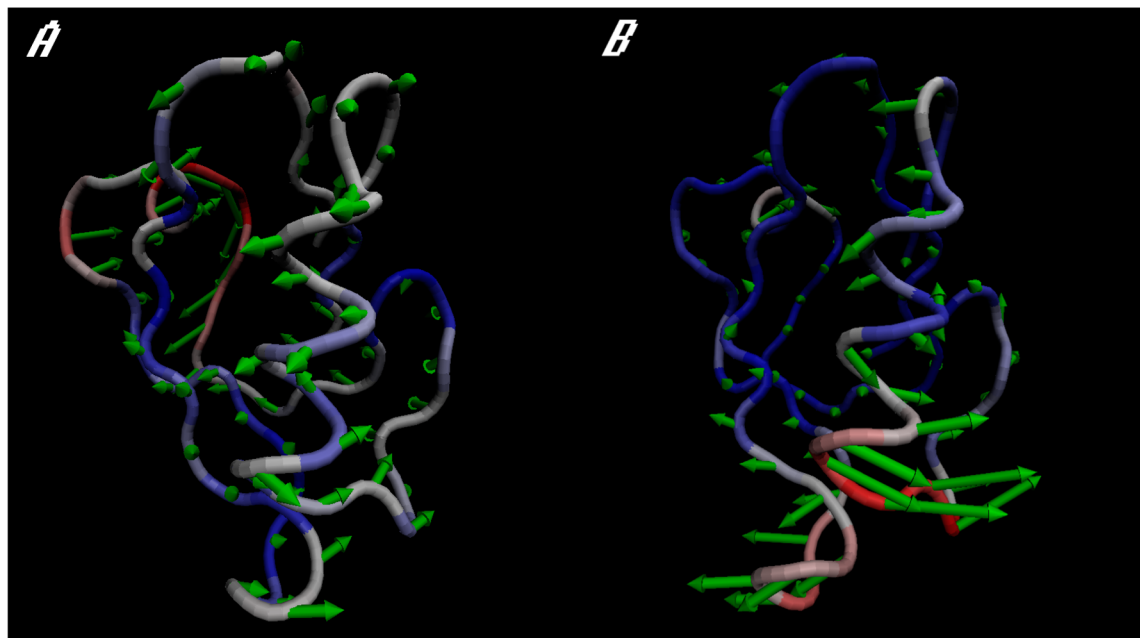


**Figure 6.** Observed protein motions represented by the projections of the first principal component (PC1) onto the protein structures of (A) ZASP<sup>WT</sup> and (B) ZASPGS4S. The differences in the protein dynamics in the target peptide binding pocket should be noted.

and ZASPGS4S. This clearly indicates that in principle the  $\alpha$ 2 helix can adopt two distinguished states, presumably to act as a flexible “gate” responsible for admission of the target peptide into the ZASP PDZ domain. The transition state between these states in the mutant was also well visible, and the populations of the conformations were almost the same in both ZASPGS4S and ZASP<sup>WT</sup>. To get more details about the individual motions of the  $\beta$ 5– $\alpha$ 2 loop and the  $\alpha$ 2 helix, we plotted the virtual dihedral angle between the C $\alpha$  atoms of residues 63–66 (the  $\alpha$ 2 helix) versus that of residues 59–62 (the  $\beta$ 5– $\alpha$ 2 loop). In ZASP<sup>WT</sup> (Figure 5A), only one concentrated cluster was observed, centered at angles of approximately 45° and -140°, respectively. In contrast, in the mutant form (Figure 5B) there were at least three linked clusters spread between  $\beta$ 5– $\alpha$ 2 loop residue dihedral angles of -140° and -70°, showing that the conformation of this region changed significantly during the cMD simulations. These changes also led to an increased mean

value of the created  $\alpha$ 2 helix virtual dihedral angle (46.2° in ZASP<sup>WT</sup> vs 50.3° in ZASPGS4S). Thus, the  $\alpha$ 2 helix is shifted toward the  $\beta$ 2 sheet in the ZASPGS4S mutant, which in fact favors the formation of the Leu17–Gln66 H-bond.

However, it is not fully clear whether after 70–120 ns of simulation we observed an adaptation of the mutant structure introduced by G54S mutation or a general structure destabilization leading to two possible conformational states depending on the occupational position of the  $\alpha$ 2 helix. Moreover, it is not obvious how these two likely conformational states are in the ZASPGS4S. To answer these questions, we ran two additional, much longer aMD and cMD simulations with lengths of 300 and 400 ns, respectively. To avoid any biases, the mutant structure obtained after 120 ns of simulation (cMD4 run) was chosen as the starting point. Initially, PCA of only the first 100 ns of the new MD runs was performed (Figure S9A,B in the Supporting Information), which

confirmed that the observed dynamical behavior was not linked to an adaptation but instead to the real dynamics of the mutated protein (see Figure S9B and Figure 4B). These figures are, in fact, identical and show two almost equally populated clusters. However, after 400 ns of simulation time (Figure S9D), the cluster representing the  $\alpha$ 2 helix conformation that is distant to the  $\beta$ 2 sheet was clearly much more populated, in accordance with the  $\alpha$ 2 helix– $\beta$ 2 sheet distance measurements (about 80% against 20%). Thus, during the sampling the  $\alpha$ 2 helix “jumps” between these conformations, but the more energetically stable conformation of ZASP<sup>G54S</sup> is different from that of ZASP<sup>WT</sup>. Much better sampling of this cMD simulation revealed that because of the mutant destabilization, the  $\alpha$ 2 helix can more easily switch its position and drop into another stable conformation. Unlike ZASP<sup>WT</sup>, it mainly occupies the second free energy conformational state (Figure S9D). The averaged structures of the initial state and those obtained after 400 ns were virtually identical. The above results were further confirmed by the 300 ns aMD simulation (Figure S9A,C). Improved sampling was observed, especially in the aMD clusters.

However, using only the PCA technique one cannot obtain information about the deviations between selected distances during the simulation time and their frequency. Thus, we plotted the above-mentioned indicative distance between the  $\alpha$ 2 helix and the  $\beta$ 2 sheet and those for the Leu17–Gln66 pair for both the wild type and the mutant (Figure S11 in the Supporting Information). It was seen that the H-bond formation strongly depends on the  $\alpha$ 2 helix conformation and that the larger distance to the  $\beta$ 2 sheet leads to H-bond formation.

Finally, the dynamics of the observed structural elements were visualized by projections of the first principal component (PC1) on the protein structures to show the amplitudes and directions of the motions (Figure 6). These results confirm all of the above conclusions and also provide a clear overview of the differences in the ZASP<sup>G54S</sup> and ZASP<sup>WT</sup> dynamics. The motion of the  $\alpha$ 2 helix and  $\beta$ 5– $\alpha$ 2 loop in ZASP<sup>G54S</sup>, taking place in the direction opposite of that of the  $\beta$ 2 sheet bottom, is well visible and is in agreement with the correlation analysis. The changes in the motion of the 40–45 region and the lifting of the G54S mutant in an upward direction are also easy detectable. Thus, the overall data suggest that the G54S mutation perturbs the  $\alpha$ 2 helix dynamics and stabilizes its position predominantly into the second likely conformational state in the protein mutant form. The opening of the bottom of the  $\alpha$ 2 helix contributes to the formation of the Leu17–Gln66 H-bond.

The above analyses demonstrate that at least 100 ns of simulation had to be performed in order to outline the differences between the ZASP<sup>WT</sup> and ZASP<sup>G54S</sup> dynamical behaviors, and MD runs of at least 100 ns are recommended for similar studies of point mutation effects. All of the MD simulations were very well reproducible even in the flexible elements (Figure S6 in the Supporting Information).

**Free Energy Calculations.** To further confirm the results, we also performed free energy calculations based on the averaged last 20 ns of each cMD. The  $\alpha$ 2 helix in ZASP<sup>G54S</sup> binds more strongly to the  $\beta$ 5– $\alpha$ 2 loop region than that in ZASP<sup>WT</sup>. The difference in binding was  $\Delta\Delta G = 2.9 \pm 0.4$  kcal/mol without consideration of the entropy contribution and was mainly due to the much stronger interactions between Met60 and the  $\alpha$ 2 helix residues Glu64 and Ala65 ( $\Delta G = 1.8 \pm 0.2$

kcal/mol). Thus, the  $\beta$ 5– $\alpha$ 2 loop attracts and shifts the bottom position of the  $\alpha$ 2 helix. An additional contribution comes from the Met60–Lys68 pair ( $\Delta\Delta G = 0.2 \pm 0.05$  kcal/mol) and from the interactions between Asp53 in the  $\beta$ 5 sheet and the Lys68–Ile69 pair in the  $\alpha$ 2 helix upper end ( $\Delta\Delta G = 0.3 \pm 0.05$  kcal/mol). Indeed, the strong perturbation of Ala65 also affects the position of Gln66 and hence the formation of the above-mentioned strong H-bond, which presumably is the most significant difference between the mutant and wild type of ZASP. The stabilization of Ala65 contributes to the stabilization of Gln66 and the formation of the Ala17–Gln66 H-bond. The Ala17–Gln66 interaction is much stronger in ZASP<sup>G54S</sup> than in the wild type, and an energy difference of  $2.1 \pm 0.4$  kcal/mol was measured. Thus, this difference is supported simultaneously by the energy calculations. Overall, the free energy data reveal in more detail the mechanism of the observed structural changes provoked by the G54S mutation and help provide a more profound explanation of the observed stronger H-bond between Leu17 and Gln66.

## ■ DISCUSSION

The NMR experimental data for the  $\alpha$ -actinin2–ZASP complex showed that Leu17 is the residue that displays a major chemical shift during formation of the complex. This residue is strongly involved in  $\alpha$ -actinin2 binding, followed by Arg16.<sup>10</sup> It has been shown also that the binding pocket consists of both the  $\beta$ 2 sheet and the  $\alpha$ 2 helix residues and that the  $\alpha$ -actinin2 C-terminal peptide binds in this groove (see Figure 5 in ref 10). This experimental observation is in agreement with our results and confirms the destructive role of the G54S mutation. Our simulations indicate that the G54S mutation can perturb the natural C-terminal peptide–ZASP interactions through the significant changes in the binding pocket and, in particular, by pulling off the  $\alpha$ 2 helix, repositioning of residues Leu17 and Arg16, and formation of the Leu17–Gln66 H-bond. All of these changes might result in reduced peptide binding as a result of the induced changes in the interactions at the bottom of the  $\alpha$ 2 helix, the restricted access caused by the above-mentioned H-bond formation, and the Arg16 displacement. In fact, residues 16 and 17 show the largest NMR chemical shifts upon peptide binding in almost all PDZ domains and especially in PDZ3 that has been proven to be important for the internal PDZ domain dynamics.<sup>26</sup> On the basis of these experimental data and our MD simulations, we propose that the observed structural and dynamics changes in the ZASP<sup>G54S</sup> PDZ domain can affect the LTCC binding too.

A significant NMR shift has been observed in the mentioned 40–45 portion, suggesting that this region can also be involved, at least indirectly, in the peptide binding.<sup>10</sup> Hence, the perturbation of this structural element observed here as a result of the G54S mutation shows that this mutation can also destabilize other regions linked to the binding site. The much larger fluctuations in the 30–40 residue segment support this hypothesis. How exactly the change in the binding site geometry influences the peptide binding (i.e., whether it leads to higher or lower binding capacity) is a subject of our further analyses that are currently ongoing. For instance, our preliminary simulations have shown that the G54S destabilization leads to a higher free energy of  $\alpha$ -actinin2–ZASP binding relative to the wild type and that even the  $\alpha$ -actinin2 C-terminal peptide can be pulled out the binding pocket (unpublished data). It has already been suggested that the  $\alpha$ 2 helix acts as a flexible gate and has a role in peptide recognition.<sup>10</sup> Our results

confirm this hypothesis. In wild-type ZASP, the  $\alpha$ 2 helix can adopt open and closed states in a ratio of up to 40% and 60%, respectively, thus allowing the peptide recognition and accommodation. However, according to our results on the mutant dynamics, the above ratio is reversed and is in the range of 20% to 80% for the closed and open states, respectively. Thus, the G54S mutation might not have some dramatic impact on the structure but significantly changes the protein dynamics at the binding site. This leads to a binding pocket that is more open and also (because of the Leu17–Gln66 H-bond) more restricted by length and most likely has impaired functions.

Perturbation of the  $\alpha$ 2 helix via other mechanisms cannot be excluded, but if any, it obviously would result in the formation of the Leu17–Gln66 H-bond. We cannot exclude the Gln66 perturbation via Asp53 that, as shown above, can affect Lys68 and/or Ile69 via Ile69–Leu78 pair interactions. It is known that ~70% of disease-associated mutations are in protein sites that most likely affect protein function.<sup>48</sup> Thus, both the experimental data and the in silico data presented here clearly show that affecting the discussed structural elements also has an impact on the target peptide binding and that the G54S mutation in ZASP is “damaging” for the protein interactions.

To the best of our knowledge, this is the first reported ZASP PDZ domain mutation that can be linked to HCM. We have relied on clinical data, and it is difficult indeed to trace out how exactly the G54S mutation in the ZASP PDZ domain can provoke hypertrophy. However, a possible explanation might be based on a recent study that identified ENH to be involved in the development of cardiac hypertrophy and to play a central role in the adaptive changes in the link between mechanical stress sensing and signaling that occurs during hypertrophy.<sup>49</sup> When overexpressed in rat neonatal cardiomyocytes, ENH1 promotes the expression of hypertrophy markers and increases the cell volume, whereas on the contrary, ENH4 overexpression prevents these changes. A path has also been proposed through which ENH can provoke cardiomyopathy.<sup>50</sup> Under stress, ENH1 could be expressed and would increase the PKC and PKD expression. Then, PKC could phosphorylate PKD1,<sup>51</sup> which itself would phosphorylate class II histone deacetylases (HDACs), thereby resulting in their dissociation from MEF2 and their binding to the chaperone protein 14-3-3 that shuttles from the nucleus to the cytoplasm.<sup>52,53</sup> This relieves the repressor effect of HDACs on MEF2, leading to activation of the hypertrophic process. HDACs can also be phosphorylated by the  $\text{Ca}^{2+}/\text{CaM}$  kinase II $\delta$ , the major cardiac isoform.<sup>54–56</sup> ZASP is a member of the enigma family and a close homologue of ENH. The sequence similarities between ZASP and enigma PDZ domains are very high and vary between 71% and 81%.<sup>10</sup> Both ZASP and ENH have been reported to bind to  $\alpha$ -actinin2, thus localizing to the Z-disk of cardiac myocytes. Because of the conservative residues in the binding site, it has been proposed that these two homologues have similar  $\alpha$ -actinin2 binding.<sup>10</sup> Moreover, both ZASP and ENH bind to the LTCC and act as kinase transporters. The role of L-type  $\text{Ca}^{2+}$  channel activation by ENH1 in the cardiomyopathy development process is currently unknown.<sup>49</sup> However, very recently it has been shown that ZASP binds to L-type  $\text{Ca}^{2+}$  via its PDZ domain and to both PKC and PKA via the LIM domains.<sup>7</sup> Most of the cardiomyopathy mutations in ZASP reported to date are linked to the LIM domains and thus are supposed to affect PKC and PKA binding.<sup>17</sup> In contrast, the LTCC binds to the PDZ domain, and the complex might be affected by its mutations.

Thus, our result that mutations in the PDZ domain can destabilize binding to the LTCC suggests a role of the G54S mutation and other PDZ ZASP mutations in the development of HCM, which may be linked to the reduced LTCC binding capability and disruption of both the PKC and PKA kinase transport to the LTCC as well as LTCC phosphorylation. However, it has been shown that ablation of LTCC Ser<sup>1928</sup> phosphorylation in a knock-in transgenic mouse model does not affect the calcium current induced by the  $\beta\text{AR}-\text{cAMP}-\text{PKA}$  signaling in mouse cardiomyocytes.<sup>57</sup> Therefore, the actual in vivo function of Cypher/ZASP as an AKAP requires further study, including the identification of the central target in the ZASP–PKA–CaN multimolecule signaling complex. Indeed, the reduced binding of  $\alpha$ -actinin2 to ZASP can play a significant role in HCM development too.

Finally, our study demonstrates that the combination of genetic screening, bioinformatics, and MD studies can be a helpful tool for classifying mutations identified as VOUS. Such an integrated approach can provide more informative and precise data than using solely single tools. Moreover, very recently it has been shown that the implication of only bioinformatics tools such as SIFT and PolyPhen-2 in the case of HCM is limited to only the major HCM-causing genes *MYH7* and *MYBPC*.<sup>23</sup> The approach also helps in discarding false-positive and -negative nsSNPs from the real disease-causing mutations and providing an explanation at molecular level about their mechanism of action. Future validation by many targets and VOUSs would be valuable. The suggested workflow can be useful for providing structural information about the impact of mutations that consequently can open the door for new treatment strategies and drug targeting. In view of the fact that nowadays MD simulations are not so greatly time-consuming and most MD codes are GPU-ported,<sup>34,35</sup> our approach can be applied to other at least small sarcomeric proteins and the simulation results can be obtained in a relatively fast and accurate manner.

## CONCLUSIONS

Hypertrophic cardiomyopathy (HCM) is an inherited heart disease that can affect people of any age and can be a reason for sudden cardiac arrest in young persons. On average, one of every 500 people has HCM. Most often HCM is caused by single-nucleotide polymorphism in genes coding for heart muscle proteins. The mechanism by which mutations can lead to HCM is not well understood. Here we suggest an approach that combines genetic screening analysis with bioinformatics and MD simulations to gain insight into the structural mechanisms that can lead to HCM. The focus of our study was the Z-disk protein ZASP (*LDB3* gene), which interacts with  $\alpha$ -actinin2 and the calcium voltage channels (LTCC) through its PDZ domain. We have reported a new ZASP PDZ mutation (Gly54Ser) and demonstrated that this mutation could significantly influence the interactions of the ZASP PDZ domain with its binding partners. Our results suggest that ZASP<sup>G54S</sup> can be linked to HCM and that the *LDB3* gene would have to be considered in the common HCM genetic tests. Our approach can also be applied to other proteins to provide structural information about the impact of mutations.

## ASSOCIATED CONTENT

### S Supporting Information

Table S1 and Figures S1–S11. This material is available free of charge via the Internet at <http://pubs.acs.org>.

## AUTHOR INFORMATION

### Corresponding Author

\*E-mail: fratev@biomed.bas.bg. Tel: +35988362716.

### Notes

The authors declare no competing financial interest.

## ABBREVIATIONS

AKAP, A-kinase anchor protein; aMD, accelerated molecular dynamics; CaN, calcineurin; cMD, classical molecular dynamics; DCM, dilated cardiomyopathy; ENH, enigma homologue protein; HCM, hypertrophic cardiomyopathy; HDAC, histone deacetylase; LTCC, L-type calcium channel; LVNC, left ventricular noncompaction cardiomyopathy; MEF2, myocyte enhancer factor-2; MRI, magnetic resonance imaging; MYH7, human cardiac myosin; MYBPC3, myosin binding protein C; PKC, protein kinase C; PKA, protein kinase A; PKD1, protein kinase D1; PSIC, position-specific independent count; RMSD, root-mean-square deviation; RMSF, root-mean-square fluctuation; SNP, single-nucleotide polymorphism; VOUS, variant of unknown significance; ZASP, Z-band alternately spliced PDZ-containing protein.

## REFERENCES

- (1) Zhou, Q.; Ruiz-Lozano, P.; Martone, M. E.; Chen, J. Cypher, a striated muscle-restricted PDZ and LIM domain-containing protein, binds to  $\alpha$ -actinin-2 and protein kinase C. *J. Biol. Chem.* **1999**, *274*, 19807–19813.
- (2) te Velthuis, A. J.; Bagowski, C. P. PDZ and LIM domain-encoding genes: Molecular interactions and their role in development. *Sci. World J.* **2007**, *7*, 1470–1492.
- (3) Zheng, M.; Cheng, H.; Li, X.; Zhang, J.; Cui, L.; Ouyang, K.; Han, L.; Zhao, T.; Gu, Y.; Dalton, N. D.; Bang, M. L.; Peterson, K. L.; Chen, J. Cardiac-specific ablation of Cypher leads to a severe form of dilated cardiomyopathy with premature death. *Hum. Mol. Genet.* **2009**, *18*, 701–713.
- (4) Arimura, T.; Hayashi, T.; Terada, H.; Lee, S. Y.; Zhou, Q.; Takahashi, M.; Ueda, K.; Nouchi, T.; Hohda, S.; Shibutani, M.; Hirose, M.; Chen, J.; Park, J. E.; Yasunami, M.; Hayashi, H.; Kimura, A. A Cypher/ZASP mutation associated with dilated cardiomyopathy alters the binding affinity to protein kinase C. *J. Biol. Chem.* **2004**, *279*, 6746–6752.
- (5) Zhou, Q.; Chu, P. H.; Huang, C.; Cheng, C. F.; Martone, M. E.; Knoll, G.; Shelton, G. D.; Evans, S.; Chen, J. Ablation of Cypher, a PDZLIM domain Z-line protein, causes a severe form of congenital myopathy. *J. Cell Biol.* **2001**, *155*, 605–612.
- (6) Cheng, H.; Zheng, M.; Peter, A. K.; Kimura, K.; Li, X.; Ouyang, K.; Shen, T.; Cui, L.; Frank, D.; Dalton, N. D.; Gu, Y.; Frey, N.; Peterson, K. L.; Evans, S. M.; Knowlton, K. U.; Sheikh, F.; Chen, J. Selective deletion of long but not short Cypher isoforms leads to late-onset dilated cardiomyopathy. *Hum. Mol. Genet.* **2011**, *20*, 1751–1762.
- (7) Lin, C.; Guo, X.; Lange, S.; Liu, J.; Ouyang, K.; Yin, X.; Jiang, L.; Cai, Y.; Mu, Y.; Sheikh, F.; Ye, S.; Chen, J.; Ke, Y.; Cheng, H. Cypher/ZASP Is a Novel A-kinase Anchoring Protein. *J. Biol. Chem.* **2013**, *288*, 29403–29413.
- (8) Kuroda, S.; Tokunaga, C.; Kiyohara, Y.; Higuchi, O.; Konishi, H.; Mizuno, K.; Gill, G. N.; Kikkawa, U. Protein–protein interaction of zinc finger LIM domains with protein kinase C. *J. Biol. Chem.* **1996**, *271*, 31029–31032.
- (9) Faulkner, G.; Pallavicini, A.; Formentin, E.; Comelli, A.; Ievolella, C.; Trevisan, S.; Bortolotto, G.; Scannapieco, P.; Salomon, M.; Mouly, V. ZASP: A new Z-band alternatively spliced PDZ-motif protein. *J. Cell Biol.* **1999**, *146*, 465–475.
- (10) Au, Y.; Atkinson, R. A.; Guerrini, R.; Kelly, G.; Joseph, C.; Martin, S. R.; Muskett, A.; Pallavicini, F. W.; Faulkner, G.; Pastore, A. Solution structure of ZASP PDZ domain; Implications for sarcomere ultrastructure and enigma family redundancy. *Structure* **2004**, *12*, 611–622.
- (11) Frank, D.; Frey, N. Cardiac Z-disc signaling network. *J. Biol. Chem.* **2011**, *286*, 9897–9904.
- (12) Bowles, K. R.; Abraham, S. E.; Brugada, R.; Zintz, C.; Comeaux, J.; Sorajja, D.; Tsubata, S.; Li, H.; Brandon, L.; Gibbs, R. A. Construction of a high-resolution physical map of the chromosome 10q22-q23 dilated cardiomyopathy locus and analysis of candidate genes. *Genomics* **2000**, *67*, 109–127.
- (13) Gerull, B.; Gramlich, M.; Atherton, J.; McNabb, M.; Trombitas, K.; Sasse-Klaassen, S.; Seidman, J. G.; Seidman, C.; Granzier, H.; Labbe, S. Mutations of TTN, encoding the giant muscle filament titin, cause familial dilated cardiomyopathy. *Nat. Genet.* **2002**, *30*, 201–204.
- (14) Moric-Janiszewska, E.; Markiewicz-Łoskot, G. Genetic heterogeneity of left-ventricular noncompaction cardiomyopathy. *Clin. Cardiol.* **2008**, *31*, 201–204.
- (15) Xing, Y.; Ichida, F.; Matsuoka, T.; Isobe, T.; Ikemoto, Y.; Higaki, T.; Tsuji, T.; Haneda, N.; Kuwabara, A.; Chen, R.; Futatani, T.; Tsubata, S.; Watanabe, S.; Watanabe, K.; Hirono, K.; Use, K.; Miyawaki, T.; Bowles, K. R.; Bowles, N. E.; Towbin, J. A. Genetic analysis in patients with left ventricular noncompaction and evidence for genetic heterogeneity. *Mol. Genet. Metab.* **2006**, *88*, 71–77.
- (16) Theis, J. L.; Bos, J. M.; Bartleson, V. B.; Will, M. L.; Binder, J.; Vatta, M.; Towbin, J. A.; Gersh, B. J.; Ommen, S. R.; Ackerman, M. J. Echocardiographic-determined septal morphology in Z-disc hypertrophic cardiomyopathy. *Biochem. Biophys. Res. Commun.* **2006**, *351*, 896–902.
- (17) Selcen, D.; Engel, A. G. Mutations in ZASP define a novel form of muscular dystrophy in humans. *Ann. Neurol.* **2005**, *57*, 269–276.
- (18) Ramaraj, R. Hypertrophic cardiomyopathy: Etiology, diagnosis, and treatment. *Cardiol. Rev.* **2008**, *16*, 172–180.
- (19) Schaub, M. A.; Boyle, A. P.; Kundaje, A.; Batzoglou, S.; Snyder, M. Linking disease associations with regulatory information in the human genome. *Genome Res.* **2012**, *22*, 1748–1759.
- (20) Kapplinger, J. D.; Landstrom, A. P.; Bos, J. M.; Salisbury, B. A.; Callis, T. E.; Ackerman, M. J. Distinguishing Hypertrophic Cardiomyopathy-Associated Mutations from Background Genetic Noise. *J. Cardiovasc. Transl. Res.* **2014**, *7*, 347–361.
- (21) Ng, P. C.; Henikoff, S. SIFT: Predicting amino acid changes that affect protein function. *Nucleic Acids Res.* **2003**, *31*, 3812–3814.
- (22) Adzhubei, I. A.; Schmidt, S.; Peshkin, L.; Ramensky, V. E.; Gerasimova, A.; Bork, P.; Kondrashov, A. S.; Sunyaev, S. R. A method and server for predicting damaging missense mutations. *Nat. Methods* **2010**, *7*, 248–249.
- (23) Fratev, F.; Jónsdóttir, S. Ó.; Pajeva, I. Structural insight into the UNC-45–myosin complex. *Proteins* **2013**, *81*, 1212–1221.
- (24) Fratev, F.; Jónsdóttir, S. Ó. An in silico study of the molecular basis of B-Raf activation and conformational stability. *BMC Struct. Biol.* **2009**, *9*, No. 47.
- (25) Fratev, F.; Piparo, E. L.; Benfenati, E.; Mihaylova, E. Toxicity study of allelochemical-like pesticides by a combination of 3D-QSAR, docking, local binding energy (LBE) and GRID approaches. *SAR QSAR Environ. Res.* **2007**, *18*, 675–692.
- (26) Feng, W.; Zhang, M. Organization and dynamics of PDZ-domain-related supramodules in the postsynaptic density. *Nat. Rev. Neurosci.* **2009**, *10*, 87–99.
- (27) NHLBI GO Exome Sequencing Project (ESP), Seattle, WA. Exome Variant Server. <http://evs.gs.washington.edu/EVS> (accessed Jan 10, 2014).
- (28) 1000K Project Database <http://www.1000genomes.org> (accessed Jan 15, 2014).
- (29) Durbin, R. M.; Abecasis, G. R.; Altshuler, R. M.; Auton, G. A. R.; Brooks, D. R.; Durbin, A.; Gibbs, A. G.; Hurles, F. S.; McVean, F. M.; Donnelly, P.; Egholm, M.; Flück, P.; Gabriel, S. B.; Gibbs, R. A.; Knoppers, B. M.; Lander, E. S.; Lehrach, H.; Mardis, E. R.; McVean, G. A.; Nickerson, D. A.; Peltonen, L.; Schafer, A. J.; Sherry, S. T.; Wang, J.; Wilson, R. K.; Gibbs, R. A.; Deiros, D.; Metzker, M.; Muzny, D.; Reid, J. A map of human genome variation from population-scale sequencing. *Nature* **2010**, *467*, 1061–1073.

- (30) Stephens, M.; Smith, N. J.; Donnelly, P. A new statistical method for haplotype reconstruction from population data. *Am. J. Hum. Genet.* **2001**, *68*, 978–989.
- (31) Sunyaev, S. R.; Eisenhaber, F.; Rodchenkov, I. V.; Eisenhaber, B.; Tumanyan, V. G.; Kuznetsov, E. N. PSIC: Profile extraction from sequence alignments with position-specific counts of independent observations. *Protein Eng.* **1999**, *12*, 387–394.
- (32) Guerois, R.; Nielsen, J. E.; Serrano, L. Predicting changes in the stability of proteins and protein complexes: A study of more than 1000 mutations. *J. Mol. Biol.* **2002**, *320*, 369–387.
- (33) Case, D. A.; Darden, T. A.; Cheatham, T. E., III; Simmerling, C. L.; Wang, J.; Duke, R. E.; Luo, R.; Walker, R. C.; Zhang, W.; Merz, K. M.; Roberts, B.; Hayik, S.; Roitberg, A.; Seabra, G.; Swails, J.; Goetz, A. W.; Kolossaváry, I.; Wong, K. F.; Paesani, F.; Vanicek, J.; Wolf, R. M.; Liu, J.; Wu, X.; Brozell, S. R.; Steinbrecher, T.; Gohlke, H.; Cai, Q.; Ye, X.; Wang, J.; Hsieh, M.-J.; Cui, G.; Roe, D. R.; Mathews, D. H.; Seetin, M. G.; Salomon-Ferrer, R.; Sagui, C.; Babin, V.; Luchko, T.; Gusarov, S.; Kovalenko, A.; Kollman, P. A. AMBER 12; University of California: San Francisco, 2012.
- (34) Pierce, L. C. T.; Salomon-Ferrer, R.; de Oliveira, C. A. F.; McCammon, J. A.; Walker, R. C. Routine access to millisecond timescale events with accelerated molecular dynamics. *J. Chem. Theory Comput.* **2012**, *8*, 2997–3002.
- (35) Le Grand, S.; Goetz, A. W.; Walker, R. C. SPFP: Speed without compromise—A mixed precision model for GPU accelerated molecular dynamics simulations. *Comput. Phys. Commun.* **2013**, *184*, 374–380.
- (36) Ryckaert, J. P.; Ciccotti, G.; Berendsen, H. J. C. Numerical integration of the Cartesian equations of motion of a system with constraints: Molecular dynamics of *n*-alkanes. *J. Comput. Phys.* **1977**, *23*, 327–341.
- (37) Petersen, H. G. Accuracy and efficiency of the particle-mesh-Ewald method. *J. Chem. Phys.* **1995**, *103*, 3668–3679.
- (38) Maestro, version 9.4; Schrödinger LLC: New York, 2013; [www.schrodinger.com](http://www.schrodinger.com).
- (39) Hamelberg, D.; Mongan, J.; McCammon, J. A. Accelerated molecular dynamics: A promising and efficient simulation method for biomolecules. *J. Chem. Phys.* **2004**, *120*, 11919–11929.
- (40) Hamelberg, D.; de Oliveira, C. A. F.; McCammon, J. A. Sampling of slow diffusive conformational transitions with accelerated molecular dynamics. *J. Chem. Phys.* **2007**, *127*, No. 155102.
- (41) Miller, B. R., III; McGee, T. D.; Swails, J. M.; Homeyer, N.; Gohlke, H.; Roitberg, A. E. MMPBSA.py: An efficient program for end-state free energy calculations. *J. Chem. Theory Comput.* **2012**, *8*, 3314–3321.
- (42) Kouskoumvekaki, I.; Petersen, R. K.; Fratev, F.; Taboureau, O.; Nielsen, T. E.; Oprea, T. I.; Sonne, S. B.; Flindt, E. N.; Jónsdóttir, S. Ó.; Kristiansen, K. Discovery of a novel selective PPAR $\gamma$  ligand with partial agonist binding properties by integrated *in silico/in vitro* work flow. *J. Chem. Inf. Model.* **2013**, *53*, 923–937.
- (43) Roe, D. R.; Cheatham, T. E., III. PTraj and CPPTRAj: Software for Processing and Analysis of Molecular Dynamics Trajectory Data. *J. Chem. Theory Comput.* **2013**, *9*, 3084–3095.
- (44) Adrian, W. R.; Shakhnovich, S.; Shakhnovich, E. I. Contribution of Selection for Protein Folding Stability in Shaping the Patterns of Polymorphisms in Coding Regions. *Mol. Biol. Evol.* **2014**, *31*, 165–176.
- (45) Cooper, G. M.; Stone, E. A.; Asimenos, G.; Green, E. D.; Batzoglou, S.; Sidow, A. Distribution and intensity of constraint in mammalian genomic sequence. *Genome Res.* **2005**, *15*, 901–913.
- (46) Li, W. H.; Wu, C. I.; Luo, C. C. Nonrandomness of point mutation as reflected in nucleotide substitutions in pseudogenes and its evolutionary implications. *J. Mol. Evol.* **1984**, *21*, 58–71.
- (47) Kormos, B. L.; Baranger, A. M.; Beveridge, D. L. A study of collective atomic fluctuations and cooperativity in the U1A–RNA complex based on molecular dynamics simulations. *J. Struct. Biol.* **2007**, *157*, 500–513.
- (48) Sunyaev, S.; Ramensky, V.; Koch, I., III; Lathe, W.; Kondrashov, A. S. Prediction of deleterious human alleles. *Hum. Mol. Genet.* **2001**, *10*, 591–597.
- (49) Lompré, A. M. Enigma in cardiac hypertrophy. *Cardiovasc. Res.* **2010**, *86*, 349–350.
- (50) Yamazaki, T.; Wälchi, S.; Fujita, T.; Ryser, S.; Hoshijima, M.; Schlegel, W. Splice variants of Enigma homolog, differentially expressed during heart development, promote or prevent hypertrophy. *Cardiovasc. Res.* **2010**, *86*, 374–382.
- (51) Rozengurt, E.; Rey, O.; Waldron, R. T. Protein kinase D signaling. *J. Biol. Chem.* **2005**, *280*, 13205–13208.
- (52) Haberland, M.; Montgomery, R. L.; Olson, E. N. The many roles of histone deacetylases in development and physiology: Implications for disease and therapy. *Nat. Rev. Genet.* **2009**, *10*, 32–42.
- (53) McKinsey, T. A.; Zhang, C. L.; Lu, J.; Olson, E. N. Signal-dependent nuclear export of a histone deacetylase regulates muscle differentiation. *Nature* **2000**, *408*, 106–111.
- (54) Backs, J.; Backs, T.; Neef, S.; Kreusser, M. M.; Lehmann, L. H.; Patrick, D. M. The  $\delta$  isoform of CaM kinase II is required for pathological cardiac hypertrophy and remodeling after pressure overload. *Proc. Natl. Acad. Sci. U.S.A.* **2009**, *106*, 2342–2347.
- (55) Backs, J.; Song, K.; Bezprozvannaya, S.; Chang, S.; Olson, E. N. CaM kinase II selectively signals to histone deacetylase 4 during cardiomyocyte hypertrophy. *J. Clin. Invest.* **2006**, *116*, 1853–1864.
- (56) Wu, X.; Zhang, T.; Bossuyt, J.; Li, X.; McKinsey, T. A.; Dedman, J. R. Local InsP3-dependent perinuclear  $\text{Ca}^{2+}$  signaling in cardiac myocyte excitation transcription coupling. *J. Clin. Invest.* **2006**, *116*, 675–682.
- (57) Lemke, T.; Welling, A.; Christel, C. J.; Blaich, A.; Bernhard, D.; Lenhardt, P.; Hofmann, F.; Moosmang, S. Unchanged  $\beta$ -adrenergic stimulation of cardiac L-type calcium channels in Cav1.2 phosphorylation site S1928A mutant mice. *J. Biol. Chem.* **2008**, *283*, 34738–34744.